

Excellent electrochemical performance of Lithium-sulfur batteries via self-standing cathode from interwoven α -Fe₂O₃ integrated carbon nanofiber networks

Avinash Raulo, Amit Gupta, Rajiv Srivastava, Bhanu Nandan



PII: S1572-6657(20)31058-4

DOI: <https://doi.org/10.1016/j.jelechem.2020.114829>

Reference: JEAC 114829

To appear in: *Journal of Electroanalytical Chemistry*

Received date: 26 August 2020

Revised date: 19 October 2020

Accepted date: 5 November 2020

Please cite this article as: A. Raulo, A. Gupta, R. Srivastava, et al., Excellent electrochemical performance of Lithium-sulfur batteries via self-standing cathode from interwoven α -Fe₂O₃ integrated carbon nanofiber networks, *Journal of Electroanalytical Chemistry* (2020), <https://doi.org/10.1016/j.jelechem.2020.114829>

This is a PDF file of an article that has undergone enhancements after acceptance, such as the addition of a cover page and metadata, and formatting for readability, but it is not yet the definitive version of record. This version will undergo additional copyediting, typesetting and review before it is published in its final form, but we are providing this version to give early visibility of the article. Please note that, during the production process, errors may be discovered which could affect the content, and all legal disclaimers that apply to the journal pertain.

Excellent Electrochemical Performance of Lithium-Sulfur Batteries via Self-Standing Cathode from Interwoven α -Fe₂O₃ Integrated Carbon Nanofiber Networks

Avinash Raulo,¹ Amit Gupta,² Rajiv Srivastava,¹ Bhanu Nandan^{1*}

¹Department of Textile Technology, Indian Institute of Technology Delhi, Hauz Khas, New Delhi 110016 (India). E-mail: nandan@textile.iitd.ac.in

²Department of Mechanical Engineering, Indian Institute of Technology Delhi, Hauz Khas, New Delhi 110016 (India).

Abstract

Lithium-sulfur batteries (LSBs) are one of the highly attractive next-generation electrochemical energy-storage systems owing to their high energy density at a low cost. However, the performance degradation of sulfur cathodes over repeated cycling remains a critical challenge to be addressed. Herein, the influence of a current collector-free and binder-free flexible self-standing cathode featured by three dimensional nanofibrous matrix composed of α -Fe₂O₃ integrated carbon nanofiber (Fe-CNF) towards improving the electrochemical performance of LSB with the aid of an effective electrolyte penetration, Li⁺ migration and accommodating the volume variation is investigated. The physical barrier effect by the interwoven nanofibrous architecture and the intense chemisorption by the combined effect of polar α -Fe₂O₃ and nitrogen-doped carbon restrict the dissolution and diffusion of soluble lithium polysulfides. In addition, the α -Fe₂O₃ ensures the acceleration of polysulfide conversion reactions. Benefiting from this architecture, the cathode retains 92.5%, of its initial capacity, after 150 cycles at 0.2 C-rate. Even

after 650 cycles at a high rate of 1 C, a significant capacity retention of 43.1% is attained, with an average capacity fade rate of 0.087% per cycle.

Keywords: Lithium-sulfur battery, Self-standing cathode, Electrospinning, Polysulfide dissolution, Catalytic effect

1. Introduction

The increasing demand of hand-held electronics as well as electric vehicles triggered the interest for developing compatible energy storage devices with high energy densities. The state-of-art lithium-ion batteries (LIBs) have been the dominant power source of such electronic devices. However, the gradual approaching theoretical performance limits ($\sim 300 \text{ mAh g}^{-1}$) owing to the relatively low capacity of the transition-metal based electrode materials used in LIBs would be unable to sustain the future demands [1,2]. Therefore, lithium-sulfur batteries (LSBs) are considered as a promising alternative due to their high theoretical capacity/energy density ($1675 \text{ mAh g}^{-1}/2600 \text{ Wh kg}^{-1}$) which results from the conversion/reconstitution based chemistry of sulfur to lithium polysulfides (Li_2S_x , $1 \leq x \leq 8$) and vice versa [3–5]. However, the practical realization of LSBs are hindered by the pronounced capacity loss with cycle number, which is resulted due to the poor electronic and ionic conductivity of both sulfur and lithium sulfides ($\text{Li}_2\text{S}_2/\text{Li}_2\text{S}$) that limit the electrochemical reactions, serious “shuttle effect” of dissolved intermediate lithium polysulfides (Li_2S_x , $4 \leq x \leq 8$, hereafter denoted as LiPS) in liquid electrolytes, large volumetric changes ($\approx 80\%$) of sulfur during repeated lithiation/delithiation process and slow reaction kinetics [6,7]. Various approaches have been undertaken to overcome these limitations, among which the most popular strategy is encapsulating sulfur within the highly conductive micro/mesoporous carbonaceous frameworks and incorporating carbonaceous interlayers that can improve the electronic conductivity of sulfur, sustain the influence of volume

expansion and inhibit LiPS dissolution [8–11]. However, the physical barrier created by the non-polar carbonaceous materials toward polar LiPS is insufficient to restrain the shuttle effect due to lack of chemical interactions. Another strategy previously reported has shown the chemical adsorption of LiPS toward polar materials and decrease of the shuttle effect [12]. Therefore, a series of polar metal oxides [13–16], metal organic frameworks [17] and polymers [18–20] have been employed as sulfur hosts, and interlayers for cathode of LSBs. In our recent work, we had presented a concept of using PEDOT-S@PAN electrospun nanofibers as the flexible additive in sulfur cathode, which was able to efficiently chemisorb the LiPS by the high surface area and polar nature of nanofibers and, thus, improved the electrochemical performance of LSB [21]. Although such polar compounds could efficiently confine the LiPS, however, the adsorbed LiPS may passively block the polar hosts during successive cycling and restrict their reuse in further cycles. Recently, substantial interest is emerging toward a more efficient strategy of using polar and catalytic materials that not only adsorb the soluble LiPS but also promote the rapid conversion of insoluble $\text{Li}_2\text{S}_2/\text{Li}_2\text{S}$ to long-chain LiPS and sulfur or vice versa, resulting in the significant improvement of capacity. One of the early studies by Salem et al. reported that the dispersion of Pt nanoparticles on graphene layer enhanced the specific capacity of LSB to 40% compared to that of the pristine graphene-based electrodes due to the electrocatalytic effect of Pt nanoparticles [22]. Besides such metallic nanoparticles, transition metal sulfides (WS_2 [23], Co_3S_4 [24]), carbides (Fe_3C [25], WC [26]), oxides ($\alpha\text{-Fe}_2\text{O}_3$ [27]) and nitrides (TiN [28], VN [29] Co_4N [30]) have gained particular interest owing to their electrocatalytic activity. Despite of the encouraging results achieved by use of such transition metal-based components, the complicated material synthesis and electrode fabrication process involved in most of these cases may restrict their adoption on the road of commercial success. Moreover, the rigid electrode

structure containing electrochemically inactive components such as binders, aluminum current collectors, and/or additional cathode interlayer etc. may reduce the specific energy density of such battery designs. Particularly, such rigid structures become incompatible for foldable and wearable electronics, where flexibility is a key concern. Therefore, it is challenging to afford a low-cost flexible electrode that simultaneously improves the polysulfide adsorption and efficiently catalyzes the LiPS conversion to boost the cycle performance of LSBs.

Based on these requirements, herein, a current collector-free and binder-free self-standing cathode using a flexible and three-dimensional network of α -Fe₂O₃ integrated carbon nanofiber matrix (Fe-CNF/S) was fabricated. Such cathode architecture provides fast electron and charge transport, accommodates the volume variation during lithiation/delithiation process, and effectively confines and catalyzes the transformation of LiPS. As a result, the sulfur utilization is significantly improved facilitating in achieving a high capacity of 1104.6 mAh g⁻¹ with 92.5% retention after 150 cycles at 0.2 C-rate, excellent rate capability with a reversible capacity of 498.5 mAh g⁻¹ at 2 C-rate, and an improved cycle stability with remarkably low capacity fade rate of 0.087% per cycle at 1 C-rate over 650 cycles.

2. Experimental section

Materials: Poly(acrylonitrile) (PAN, Mw ~ 150,000 g mol⁻¹, Sigma-Aldrich), Ferrous sulfate (heptahydrate) (FeSO₄·7H₂O, Loba Chemie), N, N-Dimethylformamide (DMF, ACS reagent, ≥99.8% Fisher Scientific), Sodium thiosulfate pentahydrate (Na₂S₂O₃·5H₂O, Merck), Hydrochloric acid (HCl, Fisher Scientific), lithium sulfide (Li₂S, Sigma-Aldrich) were used without further modification. DI water used in the experiment was doubly distilled before use. Carbon black (TIMCAL Graphite & Carbon Super P-SUP, Xiamen TOB New Energy Co. Ltd., China) was used as the conductive carbon in CB/S electrode.

Fabrication Fe-CNF and CNF nanofibrous mat: In a typical procedure, 0.1g $\text{FeSO}_4 \cdot 7\text{H}_2\text{O}$ was added in 4 ml DMF solvent and vigorously stirred at 80 °C for 12 h. Then 0.3g PAN was added to the FeSO_4 -DMF solution to reach a FeSO_4 :PAN ratio of 1:3 and stirred for another 12 h. The solution was then electrospun using a single nozzle horizontal electrospinning setup (ES-II, Espin Nanotech, India), consisting of a syringe pumps, a high voltage power supply and a drum collector wrapped with aluminum foil. All electrospinning processes were carried out under ambient conditions (25 ± 5 °C with a relative humidity of $49 \% \pm 7 \%$) by fixing the spinneret-to-collector distance and applied voltage at 11 cm and 15 kV, respectively, together with a solution flow rate of 1 mL h^{-1} . The FeSO_4 -PAN electrospun nanofiber mat was dried in air at room temperature and then carefully peeled off from the aluminum foil. Later, the nanofiber mats were thermally treated at 250 °C for 2 h with a heating rate of $5 \text{ }^\circ\text{C min}^{-1}$ in air to stabilize them, followed by carbonizing at 750 °C for 1 h in nitrogen atmosphere with same heating rate to produce $\alpha\text{-Fe}_2\text{O}_3$ -CNF (Fe-CNF). Using the same parameters equal concentration of PAN in DMF without FeSO_4 was also electrospun, and then carbonized to prepare CNF.

Fabrication of Fe-CNF/S and CNF/S electrode: The Fe-CNF nanofiber mats were punched into circular discs of diameter (Φ) = 10 mm and then soaked in a 40 wt% aqueous solution of sodium thiosulfate ($\text{Na}_2\text{S}_2\text{O}_3 \cdot 5\text{H}_2\text{O}$) containing 1% isopropanol for 2 h. The wet nanofiber discs were taken out of the solution and dipped in HCl (12 M) for 12 h followed by filtering and washing several times with DI water. Finally, the sulfur deposited Fe-CNF electrodes (Fe-CNF/S) were obtained after drying the discs in an air-oven at 50 °C overnight. The similar process was adopted to prepared sulfur deposited CNF electrodes (CNF/S).

Preparation of Li_2S_6 and symmetrical cell assembly: To prepare the 0.2 M Li_2S_6 solution, 1:5 molar ratio of Li_2S and sulfur was added into the mixture of 1,3-dioxalane and dimethoxyethane

solvent (1:1, v/v), which was then magnetically stirred in N₂ atmosphere at 60 °C for 12 h. The punched circular discs of Fe-CNF and CNF mats having $\Phi = 10$ mm as the identical working and counter electrodes with the as obtained Li₂S₆-containing electrolyte were assembled into the symmetric cell configuration for the catalytic effect analysis. The symmetrical cells without the Li₂S₆-containing electrolyte were also tested.

Materials characterization: The morphology of the electrospun nanofibers were investigated by scanning electron microscope (FE-SEM, JEOL JSM-7900F) and transmission electron microscope (TEM, Libra200, Zeiss, Germany, operated at an acceleration voltage of 200 kV). Elemental mapping results are obtained with a high-angle annular dark-field scanning transmission electron microscopy and spectrum imaging analysis based on energy-dispersive X-ray spectroscopy (HAADF-STEM and EDS). X ray diffraction (XRD) patterns were recorded on a Rigaku Ultima IV diffractometer using Cu K α radiation ($\lambda = 0.154$ nm). Thermogravimetric analysis (TGA) was conducted with a TGA 4000 (Perkin Elmer) analyzer under N₂ flow at a heating rate of 10 °C min⁻¹ to measure the amount of sulfur present in the electrode. To measure the amount of α -Fe₂O₃ present in Fe-CNF, TGA was conducted under air flow at a heating rate of 10 °C min⁻¹. The chemical states of elements were investigated by X-ray photoelectron spectroscopy (XPS) performed in an Omicron Nanotechnology XPS system (model ESCA+).

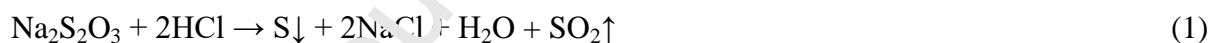
Half-cell assembly and electrochemical characterization: The Fe-CNF/S or CNF/S electrodes with areal sulfur mass loading of ~ 1 mg cm⁻² were directly used as cathode without any further treatment. The sulfur loading of each electrode was ascertained by measuring the weight of nanofiber discs ($\Phi = 10$ mm) with a high precision digital microbalance (Sartorius BSA224S-CW) before and after synthesizing sulfur. To avoid the error in electrochemical data, the electrodes of equal sulfur loadings were measured for comparison. A lithium metal foil was used

as counter and reference electrode. The liquid electrolyte was consisted of 1M bis(trifluoromethane)sulfonamide lithium salt (LiTFSI) dissolved in a mixture of 1,3-dioxolane (DOL) and 1,2-dimethoxymethane (DME) (1:1 by volume) with 1% LiNO₃ (TOB New Energy). Controlled amount of electrolyte was dropped onto the cathode by maintaining an electrolyte/sulfur (E/S) ratio of $\sim 10 \mu\text{L mg}^{-1}$. A Whatman glass fiber paper wetted by controlled amount of liquid electrolyte ($\sim 14 \mu\text{L cm}^{-2}$) was used as separator. Therefore, the overall electrolyte content with respect to the mass of sulfur was $\sim 50 \mu\text{L mg}^{-1}$. All are assembled in CR2016 coin cells in an inert atmosphere glove box with the concentration of moisture and oxygen below 0.1 ppm. For comparison, a conventional electrode (denoted as CB/S) was prepared via slurry casting method, in which a slurry of synthesized sulfur (method of synthesis explained in supplementary information), conductive carbon black (super P) and polyvinylidene fluoride (PVDF) binder with mass ratio of 5.5:3.5:10 in N-Methyl-2-pyrrolidone (NMP) was uniformly coated on an aluminum foil with a doctors blade, to control the areal sulfur mass loading of $\sim 1 \text{ mg cm}^{-2}$ in a punched electrode of $\Phi = 10 \text{ mm}$. Then the CB/S electrode was dried at 60 °C for 12 h and assembled in a coin cell using the same method as that of Fe-CNF/S electrode. The electrochemical measurements including the cyclic voltammetry (CV) test at a scan rate of 0.1 mV s^{-1} , electrochemical impedance spectroscopy (EIS) in the frequency range of 100 kHz to 10 mHz with an AC voltage amplitude of 5.0 mV under the open-circuit condition and galvanostatic discharging-charging in the potential range of 1.7 to 2.8 V (vs Li/Li⁺) at ambient temperature were performed using a Bio Logic VMP3 electrochemical workstation. The current in the galvanostatic tests were varied from 0.1 C to 2 C-rate, where the current rate were calculated based on the theoretical capacity of sulfur (i.e. $1 \text{ C} = 1675 \text{ mA g}^{-1}$) and the obtained

specific capacities mentioned in this article were calculated based on sulfur mass of the electrode.

3. Results and discussion

The overall method for the preparation of Fe-CNF/S self-standing cathode mainly involves three steps: (i) fabrication of composite nanofiber matrix by electrospinning, (ii) carbonization, and (iii) synthesis of sulfur over the nanofiber matrix, as schematically illustrated in Fig. 1. As the starting material, a solution of FeSO₄ and polyacrylonitrile (PAN) was co-electrospun to fabricate FeSO₄-PAN nanofiber mat. The nanofiber mat was then stabilized at 250 °C in air followed by carbonization at 750 °C in nitrogen atmosphere which led to the conversion of PAN to N-doped carbon and the dehydration followed by decomposition of FeSO₄ to generate α-Fe₂O₃ (as discussed in Fig. S1, Supporting Information.). Finally, the Fe-CNF nanofiber mat was cut into circular discs of 10 mm diameter and later, immersed in an aqueous solution of Na₂S₂O₃ followed by HCl treatment. This resulted in the synthesis of sulfur over the nanofibers (Fe-CNF/S) through the reaction as shown in equation 1 [31]:



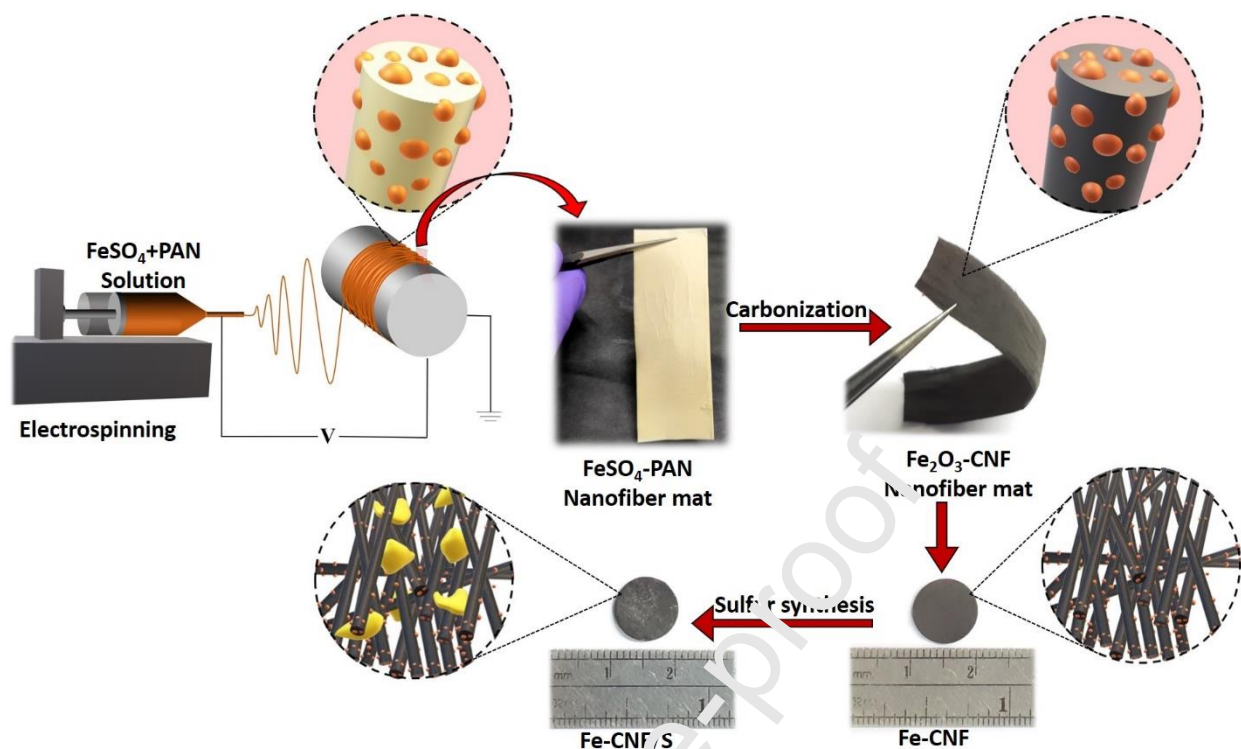


Fig. 1. Schematic illustration of the fabrication process of flexible Fe-CNF/S electrode.

The structural evolution throughout the fabrication process was characterized by scanning electron microscopy (SEM), transmission electron microscopy (TEM), energy-dispersive X-ray spectroscopy (EDS) elemental mapping and X-ray diffraction (XRD). The typical SEM image (Fig. 2a) clearly displays that the Fe-CNFs exist as interwoven structure with average fiber diameter of about 200-300 nm. In contrast to the CNF (Fig. S2, supplementary information), the Fe-CNF exhibited a rough surface (inset of Fig. 2a) plausibly due to the presence of $\alpha\text{-Fe}_2\text{O}_3$ nanoparticles. The homogeneous distribution of $\alpha\text{-Fe}_2\text{O}_3$ across the nanofiber integrated with carbon was observed by TEM (Fig. 2b). This was further revealed by the HAADF-STEM image (Fig. 2c) and the corresponding EDS maps (Fig. 2 d-g) of Fe, O, N and C displaying the distribution of Fe and O throughout the N-doped CNF. The content of $\alpha\text{-Fe}_2\text{O}_3$ in Fe-CNF

networks was 19.6% as measured by the TGA thermogram (Fig. S3, supplementary information).

After immersion of Fe-CNF matrix in aqueous solution of $\text{Na}_2\text{S}_2\text{O}_3$ followed by HCl treatment, the as obtained Fe-CNF/S electrode showed the presence of sulfur aggregates throughout the interwoven Fe-CNF matrix (Fig. 2h). The average thickness of the electrode was measured to be $\sim 300 \pm 10 \mu\text{m}$ (Fig. 2i). Apparently, identical morphology was also observed in case of similar size CNF/S electrode prepared by following the same method (Fig. S4, supplementary information). The XRD patterns of FeSO_4 -PAN, Fe-CNF and Fe-CNF/S were also analyzed to probe the crystal structure and phase purity, as displayed in Fig. 2j. The sharp intense peak at 17.6° in FeSO_4 -PAN nanofiber corresponding to the (100) crystalline plane of the PAN [32] disappeared after carbonization. A broad peak at about 25° appeared in Fe-CNF due to the formation of amorphous carbons, along with additional sharp peaks at 33.14° and 35.67° corresponding to the (104) and (110) facets of $\alpha\text{-Fe}_2\text{O}_3$, respectively [33]. The negligible intensities of other peaks were mainly due to the low fraction of the $\alpha\text{-Fe}_2\text{O}_3$ and, hence, scattering intensity was dominated by that from the amorphous carbon in the nanofibers. On the other hand, CNF did not display such diffraction peaks of $\alpha\text{-Fe}_2\text{O}_3$ (Fig. S5, supplementary information). For Fe-CNF/S, the well-defined crystalline peaks of orthorhombic sulfur were distinctly identified that confirmed the successful synthesis of sulfur over the nanofibers [31]. The weight content of sulfur present in Fe-CNF/S determined by thermogravimetric analysis (TGA) is about 54% of the whole electrode, that corresponds to a mass loading of $\sim 1 \text{ mg cm}^{-2}$ (Fig. S6, supplementary information). The sulfur content can be tuned by altering the concentrations of $\text{Na}_2\text{S}_2\text{O}_3$ in the aqueous solution and HCl during the synthesis process.

However, a uniform mass loading of sulfur was maintained throughout the experiment for accurate comparison and analysis.

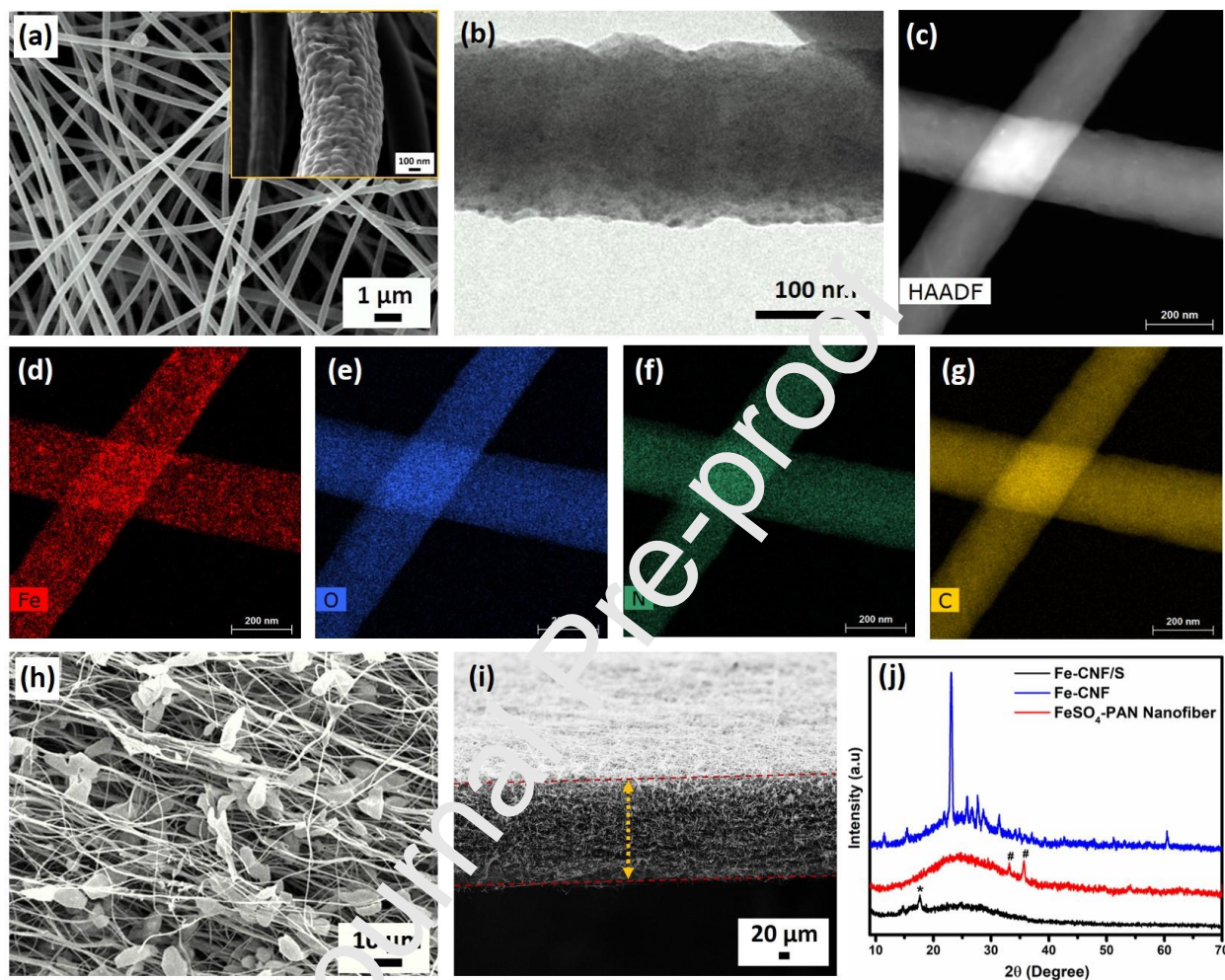


Fig. 2. (a) SEM image of Fe-CNF with the inset representing the image at high magnification; (b) TEM and (c) HAADF-STEM image of Fe-CNF with (d-g) corresponding elemental mapping of Fe, O, N and C; (h) Top view and (i) cross-section of Fe-CNF/S electrode; (j) XRD patterns of FeSO₄-PAN nanofiber, CNF and Fe-CNF with ‘#’ symbol correspond to the pattern of α-Fe₂O₃ and ‘*’ symbol correspond to the pattern of PAN.

X-ray photoelectron spectroscopy (XPS) measurements were carried out to obtain more detailed evidence of surface information including the elemental composition and oxidation states of Fe-

CNF/S electrode, as illustrated in Fig. 3. The survey spectrum of Fe-CNF/S (Fig. 3a) reveals the presence of C, N, O, Fe and S elements. The fitted C 1s spectrum (Fig. 3b) shows a major peak at 284.3 eV corresponding to C=C/C—C and two minor peaks at 285.7 and 288.0 eV representing C—O/C—N, and C=O bonds, respectively [34]. This indicates that carbon in Fe-CNF/S electrode surface is mostly in graphitic form with a few containing nitrogen/oxygen functional groups. The N 1s spectrum (Fig. 3c) can be resolved into three components centered at 398.0, 400.0 and 402.0 eV representing the pyridinic, pyrrolic and graphitic type of N atoms doped in the graphitic carbon of the Fe-CNF [35,36]. Such inherently doped N was formed due to the carbonization of N-enriched PAN as the carbon precursor. Previous studies have reported that the pyridinic and pyrrolic type N-dopants could provide stronger binding energies with soluble LiPS. Especially, the pyridinic N have a strong attraction with Li^+ of LiPS that lead to the strong chemisorption towards LiPS [37]. The high resolution Fe 2p spectrum (Fig. 3d) shows two main peaks centered at 711.3 eV and 724.6 eV, corresponding to Fe 2p_{3/2} and Fe 2p_{1/2}, respectively, together with a satellite peak at 719.0 eV, which further verifies that Fe present in Fe-CNF/S is in the form of $\alpha\text{-Fe}_2\text{O}_3$ [27]. In the S 2p core-level (Fig. 3e), the doublet peak at 163.2 and 164.4 eV, correspond to S-S bond and the peak at 168.5 eV can be ascribed to the sulfate species [14,34,38]. In comparison to Fe-CNF/S electrode, the CNF/S electrodes also displays the peaks of C, N, O and S element except Fe in the XPS survey spectrum (Fig. 3f).

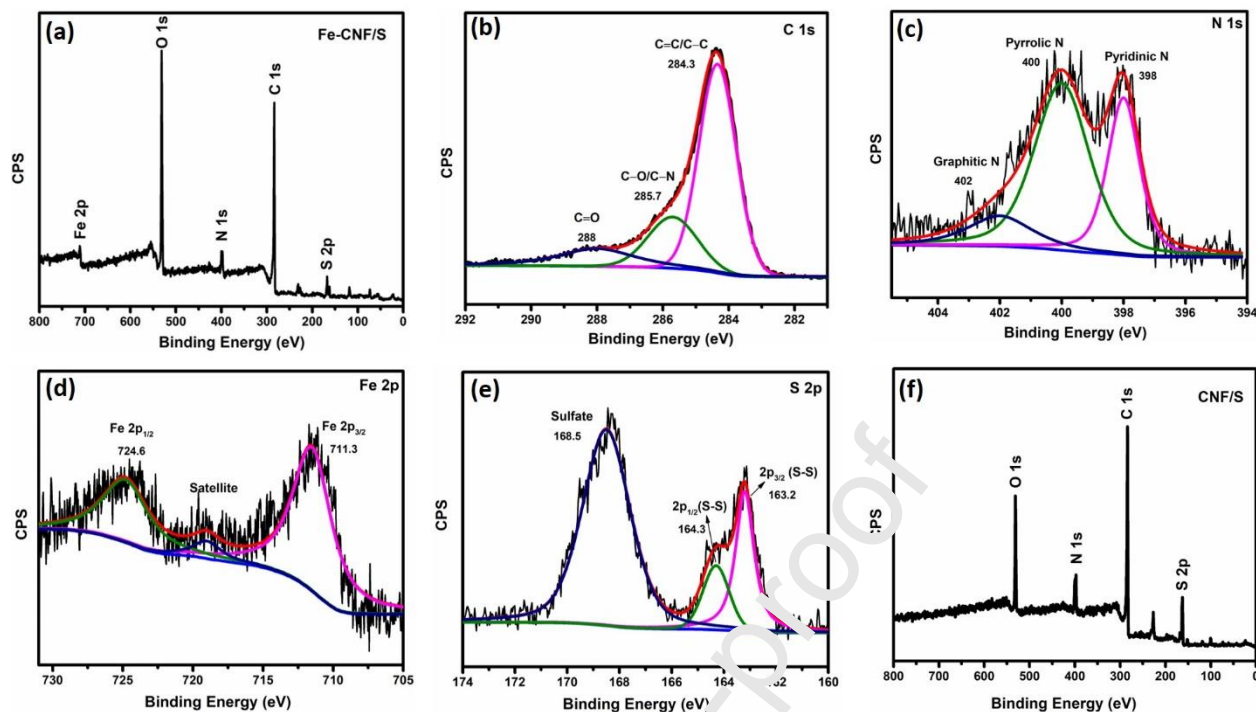


Fig. 3. (a) XPS survey spectrum of Fe-CNF/S electrode and corresponding high-resolution spectra of (b) C 1s, (c) N 1s, (d) Fe 2p, and (e) S 2p; (f) XPS survey spectrum of CNF/S.

In order to quantify the efficacy of the designed Fe-CNF/S electrode for LSB, electrochemical performances were evaluated in a 2016 coin-cell configuration with metallic lithium foil as the counter and reference electrode. The typical cyclic voltammetry (CV) curve of Fe-CNF/S electrode for the initial five cycles at a scan rate of 0.1 mV s^{-1} is shown in Fig. 4a. Two cathodic peaks are observed at $\sim 2.32 \text{ V}$ and 2.02 V , corresponding to the electrochemical reduction of sulfur to higher order LiPS (Li_2S_x , $4 \leq x \leq 8$) and the subsequent $\text{Li}_2\text{S}_2/\text{Li}_2\text{S}$, respectively. The anodic peak at $\sim 2.42 \text{ V}$ represents the electrochemical oxidation that led to the reversion of $\text{Li}_2\text{S}_2/\text{Li}_2\text{S}$ to higher order LiPS and sulfur [21]. It is interesting to note the well overlapped CV curves during scanning, which is an indication of high electrochemical reversibility of Fe-CNF/S electrodes, signifying its potential for use as LSB cathode. Thereafter, the galvanostatic discharge-charge cycling performance of the Fe-CNF/S electrode at 0.2 C-rate over the potential

range of 1.7–2.8 V was measured. For comparison, cycling performance of CNF/S electrode as controlled sample was evaluated. The electrochemical performance of a conventional electrode prepared by slurry coating method, denoted as CB/S, was compared as well to ascertain the advantage of self-standing interwoven nanofiber architectures of Fe-CNF/S and/or CNF/S electrodes. The cycling performance the three electrode configurations are displayed in Fig. 4b. The Fe-CNF/S electrode delivered a higher initial discharge capacity of 1104.6 mAh g⁻¹ and a reversible capacity of 1022.0 mAh g⁻¹ at 150th cycles, corresponding to a capacity retention of 92.5%. Though the CNF/S electrode also exhibited a similar cycling performance with capacity retention of 92.4% after 150 cycles, a low initial discharge capacity of 803.7 mAh g⁻¹ was attained. By comparison, CB/S electrode showed a severe capacity decay with a capacity retention of about 40.5% of the initial discharge capacity (773.3 mAh g⁻¹) after 150 cycles. The impressive cycle performances exhibited by the self-standing electrodes (Fe-CNF and CNF/S) compared to the conventional slurry coated electrode indicate the beneficial effect of the interwoven nanofibrous architecture, which have combined merits of efficient electrolyte penetration through the inter-fiber voids to proceed the electrochemical reactions and provide a physical barrier against the diffusion of soluble LiPS. Additionally, the N-doping in the carbon nanofibers have improved the interaction with LiPS and prevent the shuttling effect [37,39]. Furthermore, the N-doped carbon has beneficial effect for the polysulfide conversion as reported elsewhere [40,41]. Noticeably, the higher specific capacities attained in case of Fe-CNF/S electrode relative to CNF/S and CB/S electrodes, confirms the improved reaction kinetics, which is attributed to the presence of polar α -Fe₂O₃ in combination with the N-doped carbon that provide a dual chemisorption effect to strongly suppress the LiPS migration and act as a redox mediator to boost the sulfur utilization during cycling. The contribution of Fe-CNF matrix to the

capacity of Fe-CNF/S electrode could be ignored due to the low specific capacity of Fe-CNF in the potential range of 1.7V to 2.8V (Fig. S7, supplementary information). Indeed, the synthesized large sulfur aggregates present in the uncycled self-standing electrodes have inadequate contact with the nanofiber surface and therefore, weakly trapped in the interwoven nanofiber matrix. As a result, the self-standing electrodes experienced an inevitable loss of LiPS in the initial redox process, which led to capacity fading during the first 20 cycles. Owing to the step-by-step activation of large-sized sulfur aggregates on cycling, the sulfur/LiPS formed in the redox process could likely rearranged uniformly over the nanofiber surfaces into an electrochemically more favorable state, which provide sufficient sites for the efficient utilization of active materials. Therefore, after initial cycling, an increase in capacity values was observed which stabilizes on further cycling. Moreover, both the self-standing electrodes exhibit some fluctuating cycling behavior, the reason for which is not yet ascertained, and further studies need to be carried out to manifest this phenomenon.

The contribution of α -Fe₂O₃ exerted to improve electrochemical performance are evidenced by the EIS measurements before cycling and after 150 cycles at open-circuit voltage as shown in Fig. 4c and 4d, respectively. The Nyquist plots with fitting line corresponding to the equivalent circuit is shown in Fig. S8a and b (supplementary information). The equivalent circuit was consisting of the parameters, R_e representing the ohmic impedance, R_s is the resistance of the passivation film formed after cycling, R_{ct} is the charge transfer resistance, CPE_1 and CPE_2 are the constant phase elements and Z_w is the Warburg resistance (Fig. S8c, supplementary information). The impedance values of the parameters based on the model fitting are depicted in Table S1 (supplementary information). The Nyquist plots of the electrodes before cycling (Fig. 4c) are composed of semicircles in the high-medium frequency region, the diameter of which represents

the charge-transfer resistance (R_{ct}) at the electrode/electrolyte interface, and an inclined line at low frequency referring to the Warburg impedance (Z_w) that correspond to the diffusion of Li^+ . The significantly lower R_{ct} of Fe-CNF/S electrode (39.23 Ω), among all the three electrodes (92.55 Ω for CNF/S and 158.22 Ω for CB/S), confirm the improved charge transfer process at Fe-CNF/S/electrolyte interface compared to CNF/S/electrolyte and CB/S/electrolyte interface. The steepest slope in the linear portion of the Fe-CNF/S electrode, implies better electrolyte wettability due to which the diffusion of Li^+ was eventually improved [42,43]. After 150 cycles (Fig. 4d), the evolution of obvious semicircle at high frequency region for all the electrodes are ascribed to the formation of passivation film of insoluble Li_2S_2 and Li_2S (R_s), followed by a medium-frequency semicircle associated with the R_{ct} [44, 45]. Interestingly, the Nyquist plot after 150 cycles also reveals a smaller R_{ct} for Fe-CNF/S electrode (15.64 Ω) compared to CNF/S (25.18 Ω) and CB/S (32.96 Ω) electrode, demonstrating the presence of α - Fe_2O_3 in Fe-CNF backbone assist a superb charge transfer process across the electrode/electrolyte interface and potentially promote the electrochemical kinetics.

Fig. 4e display the galvanostatic charge-discharge profiles at 0.2 C-rate of the three kind of electrode configurations (Fe-CNF/S, CNF/S and CB/S) at 150th cycle. The two typical voltage plateaus during discharge can be observed for all the three configurations, which represents the sequential electrochemical reduction of sulfur and the galvanostatic charge profile corresponding to the electrochemical oxidation of LiPS. The upper discharge plateau at ~ 2.35 V is associated with the formation of soluble LiPSs (Li_2S_x , $4 \leq x \leq 8$) that originate the shuttle effect and the lower discharge plateau at ~ 2.1 V is ascribed to the formation of the insoluble sulfides of Li_2S_n ($n = 1, 2$). The comparison in the ratio of discharge capacities over the lower discharge plateau region (Q_{low}) to the higher discharge plateau region (Q_{high}) is a representative of the shuttle effect

in corresponding LSBs, regardless of the error caused by the weight of sulfur in the cathode. The higher $Q_{\text{low}}/Q_{\text{high}}$ ratio of Fe-CNF/S electrode (2.74) in contrast to that of CNF/S (2.56) and CB/S (2.45) suggest that the LiPSs can be effectively trapped with suppressed shuttle effect that contribute to a high capacity in Fe-CNF/S electrode [46,47]. Apparently, a relatively low electrochemical polarization value (ΔE) of 0.24 V is observed for the Fe-CNF/S electrode as compared to those for the CNF/S (0.26 V), CB/S (0.3 V) electrodes, which showed wider potential gaps between the discharge and charge curves. This indicates that the Fe-CNF/S can improve the electrochemical reaction dynamics in LSBs [15,42].

The rate performance of the electrodes are the direct consequences of the reaction kinetics. Therefore, the rate capability of Fe-CNF/S, CNF/S and CB/S electrodes under various current rates from 0.2 C to 2 C are shown in Fig. 4f. The Fe-CNF/S electrode exhibit discharge capacities of 1138.4 mAh g⁻¹, 795.7 mAh g⁻¹, 641.8 mAh g⁻¹ and 498.5 mAh g⁻¹ at 0.2, 0.5, 1 and 2 C, respectively, followed by the recovery of a discharge capacity of 806.1 mAh g⁻¹ once the current rate was reduced back to 0.2 C. However, the CNF/S and CB/S electrode exhibit much lower discharge capacities than Fe-CNF/S under all the current rates, which suggest the fast reaction kinetics in Fe-CNF/S electrode. A similar trend in behavior of the electrodes was also observed for the long term cycling performance at a high current rate of 0.5 C as illustrated in Fig. 4g. The discharge capacity of Fe-CNF/S electrode reached to 867.2 mAh g⁻¹ with a reversible capacity of 625.7 mAh g⁻¹ after 250 cycles, corresponding to a capacity retention of ~72.1% with a high Columbic efficiency of 98%. In contrast, the CNF/S and CB/S cathodes exhibited low initial discharge capacities and delivered reversible capacities of 330.1 mAh g⁻¹ and 209.8 mAh g⁻¹, respectively after 250 cycles that corresponded to respective capacity retentions of 65.1% and 45.6%.

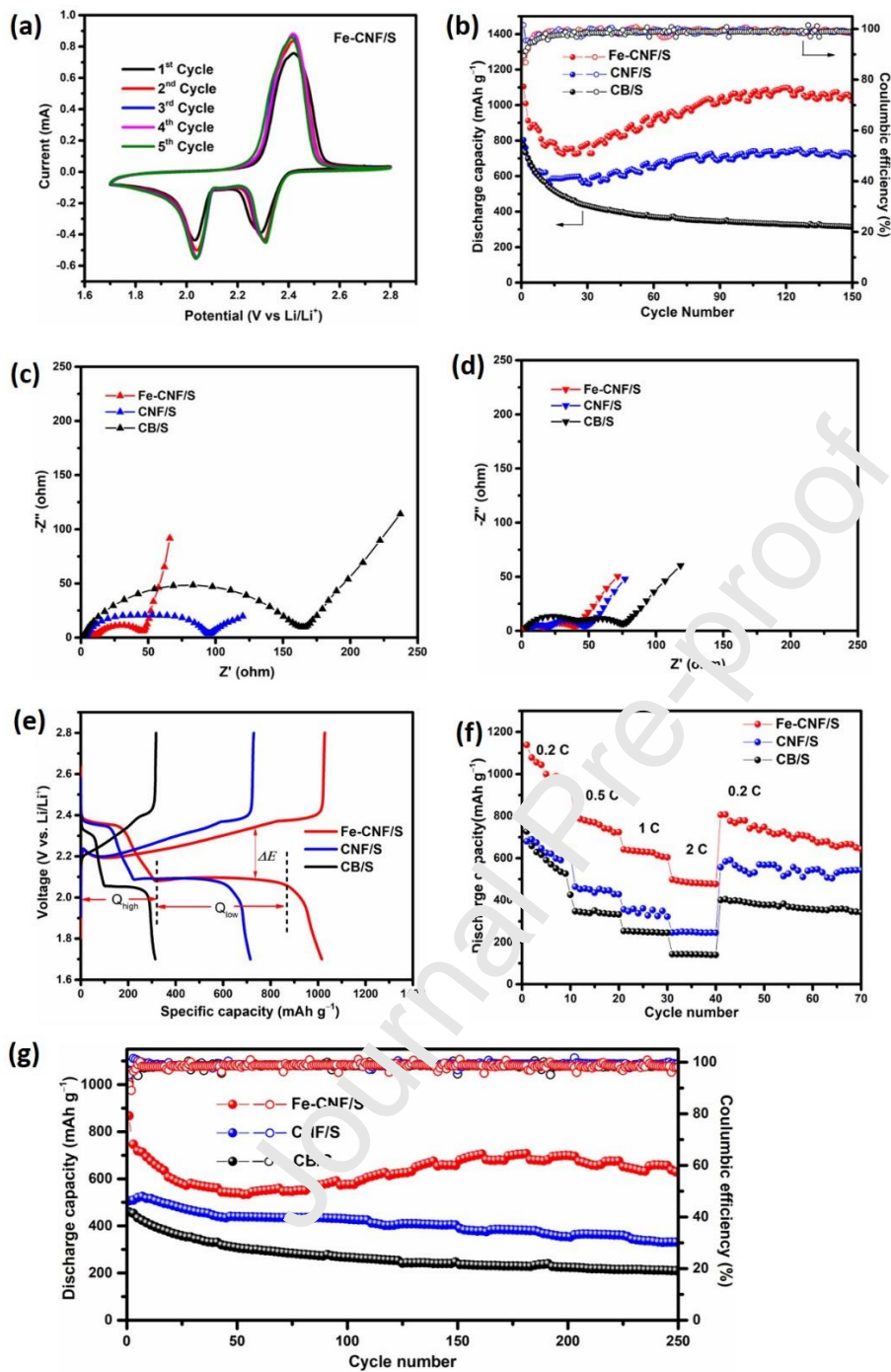


Fig. 4. (a) CV curves of Fe-CNF/S electrode at a scan rate of 0.1 mV s^{-1} ; Electrochemical performance of LSBs with Fe-CNF/S, CNF/S and CB/S electrode configurations representing the (b) Cycle performance at current rate of 0.2 C-rate; Nyquist plot (c) before cycling and (d) after

150 cycles of discharging-charging at 0.2 C; (e) 150th discharge-charge profiles at 0.2 C-rate; (f) Rate performance from 0.2 to 2 C-rate; (g) Cycling performance at a current rate of 0.5 C-rate.

To gain insight into the intrinsic role of electrode architecture towards improving the performance of LSB, post-cycling characterizations were carried out after 50 cycles of discharging-charging at 0.2 C-rate. The SEM images of fully discharged Fe-CNF/S (Fig. 5a) and CNF/S (Fig. 5b) electrodes after 50 cycles shows the existence of solid $\text{Li}_2\text{S}_2/\text{Li}_2\text{S}$ aggregates trapped in the interwoven nanofiber matrix. In contrast to the CNF/S electrode displaying solid aggregates with numerous free sites on the surface of CNF matrix, the Fe-CNF/S electrode shows a dense morphology with $\text{Li}_2\text{S}_2/\text{Li}_2\text{S}$ anchored all throughout the nanofibers of Fe-CNF matrix. The elemental mapping of the cycled Fe-CNF/S electrode (Fig. S9, supplementary information) displaying the pronounced signal of S and Fe also reveals the homogeneous distribution of sulfides across the Fe-CNF. These results highlight the importance of $\alpha\text{-Fe}_2\text{O}_3$ to uniformly deposit the discharge products, which is ascribed to the more efficient interaction of LiPSs with the Fe-CNF as compared to CNF. This interaction between LiPS and Fe-CNF was further verified by the XPS analysis. The full spectrum of cycled Fe-CNF/S and CNF/S electrodes (Fig. 5c) show the obvious presence of C, O, N, S along with additional peak of F 1s which is arising due to the remnant LiTFSI salt present in the electrolyte, and Li 1s due to the formation of LiPS during the cycling. The Fe 2p spectra (Fig. S10a, supplementary information) of Fe-CNF/S completely diminished after cycling, which is possibly due to the accumulation of a layer of LiPS on $\alpha\text{-Fe}_2\text{O}_3$. This is further evidenced by the high-resolution N 1s spectrum (Fig. S10b, supplementary information) showing a negative shift in pyrrolic N and reduction in pyridinic N intensity confirming the effective adsorption of LiPSs over the Fe-CNF [49]. This clearly demonstrates the strong chemisorption of Fe-CNF toward LiPS by the combined effect of

polar α -Fe₂O₃ and N-doped carbon. Furthermore, the S 2p spectrum of the cycled electrodes (Fig. 5d) display two peaks at 162.1 eV and 163.4 eV corresponding to the terminal sulfur (S_T^{-1}), which is likely due to the presence Li-S bond, and bridging sulfur (S_B^0) due to the S-S bonds, respectively, of the LiPS [49,50]. The additional peaks located between the binding energies of 166.0 eV and 170.0 eV is possible due to the existence of SO_x^{2-} species resulting from the reaction of sulfur with the nitrates of the electrolyte, and remaining LiTFSI [51,52]. Notably, the more intense peaks of Li-S and S-S bonds in the Fe-CNF/S compared to CNF/S electrode indicates the improved polysulfide retention by Fe-CNF due to the combined chemisorption effect of α -Fe₂O₃ and N-doped carbon. In contrast, only N-doped carbon is the dominant source for LiPS chemisorption in case of CNFs. Moreover, the morphology of Fe-CNF/S electrode is maintained even after 150 cycles of discharging/charging at 0.2 C-rate (Fig. S12, supplementary information), proving that the Fe-CNFs afford sufficient sites for the uniform distribution and strong chemisorption of LiPS.

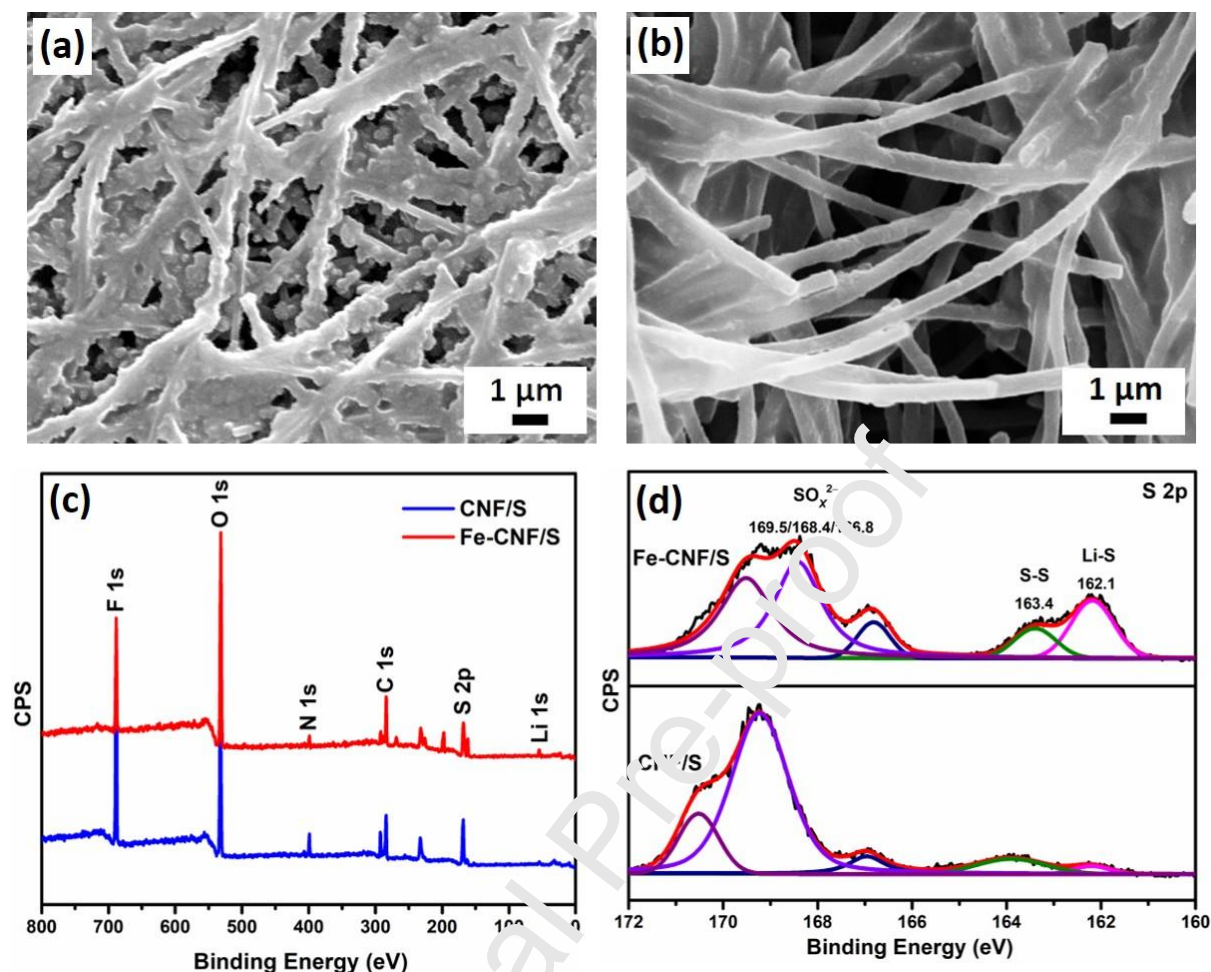


Fig. 5. SEM image after 50 cycles of (a) Fe-CNF/S and (b) CNF/S electrode; (c) XPS survey spectra, and (d) high-resolution S 2p spectrum of CNF/S and Fe-CNF/S electrodes after cycling.

In order to further analyze the underlying mechanism for the improvement of electrochemical performance in case of Fe-CNF/S compared to CNF/S, the polysulfide conversion capability of both Fe-CNF and CNF matrices was precisely analyzed by assembling coin cells in symmetric configuration with identical working and counter electrodes of the nanofiber matrices in 0.2 M Li_2S_6 electrolyte. The symmetric cells without Li_2S_6 electrolyte were also tested. The CV of Fe-CNF and CNF symmetric cells were conducted at a scan rate of 10 mV s^{-1} , within a voltage range of -1.5 to $+1.5 \text{ V}$ (vs Li/Li^+) as shown in Fig. 6a and 6b, respectively. The CV curves

showing negligible current densities for the symmetric cells without Li_2S_6 clearly demonstrates that the polarization profiles are mainly derived from the redox current of Li_2S_6 and the role of capacitive current of symmetrical electrodes is negligible [53]. For symmetric cells with Li_2S_6 , nearly overlapping CV curves of Fe-CNF exhibiting a pronounced reduction peak at -0.51 V arise from the reduction of Li_2S_6 to $\text{Li}_2\text{S}/\text{Li}_2\text{S}_2$ on the working electrode. This is followed by oxidation of $\text{Li}_2\text{S}/\text{Li}_2\text{S}_2$ to reconstitute Li_2S_6 at 0.02 V, which further oxidizes to form sulfur at 0.53 V and then reduction of sulfur to Li_2S_6 at -0.06 V (Fig. 6a) [54]. The CNF electrode also exhibited identical peaks at -0.72 V, 0.31 V, 0.77 V and -0.27 V as broad redox features (Fig. 6b). However, the sharp redox peaks with higher current densities of Fe-CNF symmetrical cell as compared to CNF symmetrical cell indicate that the presence of $\alpha\text{-Fe}_2\text{O}_3$ can potentially improve the electrochemical reversibility and polysulfide conversion. The EIS measurement conducted on the symmetrical cells (Fig. 6c) further confirms the excellent electronic conductivity of Fe-CNF. This resulted from the rapid polysulfide conversion, which led to enhanced diffusion of solvated Li^+ in the bulk of electrode and, consequently, increases the electronic movement in the interconnected N-doped carbon networks. To corroborate the above analysis, determination of Li^+ diffusion coefficients is essential. Therefore, the CV curves of Fe-CNF/S and CNF/S electrodes in half-cell configuration were further acquired under increasing scan rates from 0.1 mV s^{-1} to 0.5 mV s^{-1} as shown in Fig. 6d and 6e, respectively. It is clearly observed that the values of cathodic and anodic current peaks (A, C1, C2) for both the electrodes increases with increase in scan rate. The Li^+ diffusion coefficient (D_{Li^+}) can be estimated from the peak current (I_p) and square root of scan rate ($v^{1/2}$) using the classical Randles–Sevcik equation (equation 2):

$$I_p = 2.69 \times 10^5 \eta^{3/2} S D_{\text{Li}^+}^{1/2} C_{\text{Li}^+} v^{1/2} \quad (2)$$

where, η is the number of electrons transferred, S is the area of electrode and C_{Li^+} is the concentration of Li^+ . When η , S and C_{Li^+} are constant in a particular cell configuration, equation 2 depicts a linear relationship between the I_p and $v^{1/2}$ with the slope representing the magnitude of D_{Li^+} . In this regard, the cathodic peak current (I_{pA}) and anodic peak current (I_{pC1} , I_{pC2}) values are plotted with respect to the $v^{1/2}$ (Fig. 6f–h), which shows a linear relationship, consistent with the theoretical predictions. The Fe-CNF/S electrode exhibit larger slopes for all the three current peaks corresponding to higher D_{Li^+} values than the CNF/S electrode. This resulted due to the fast conversion of higher-order LiPS to $\text{Li}_2\text{S}_2/\text{Li}_2\text{S}$ in Fe-CNF/S electrode, that provide a driving force for the movement of Li^+ towards the electrode and consequently decrease the dissolution of LiPS in the liquid electrolyte [24]. Moreover, the electrochemical analysis of symmetrical cells along with the investigation of Li^+ diffusion in the half cells highlight the catalytic effect of Fe-CNF, which is the explicit reason for the superior battery performance in case of Fe-CNF/S electrodes.

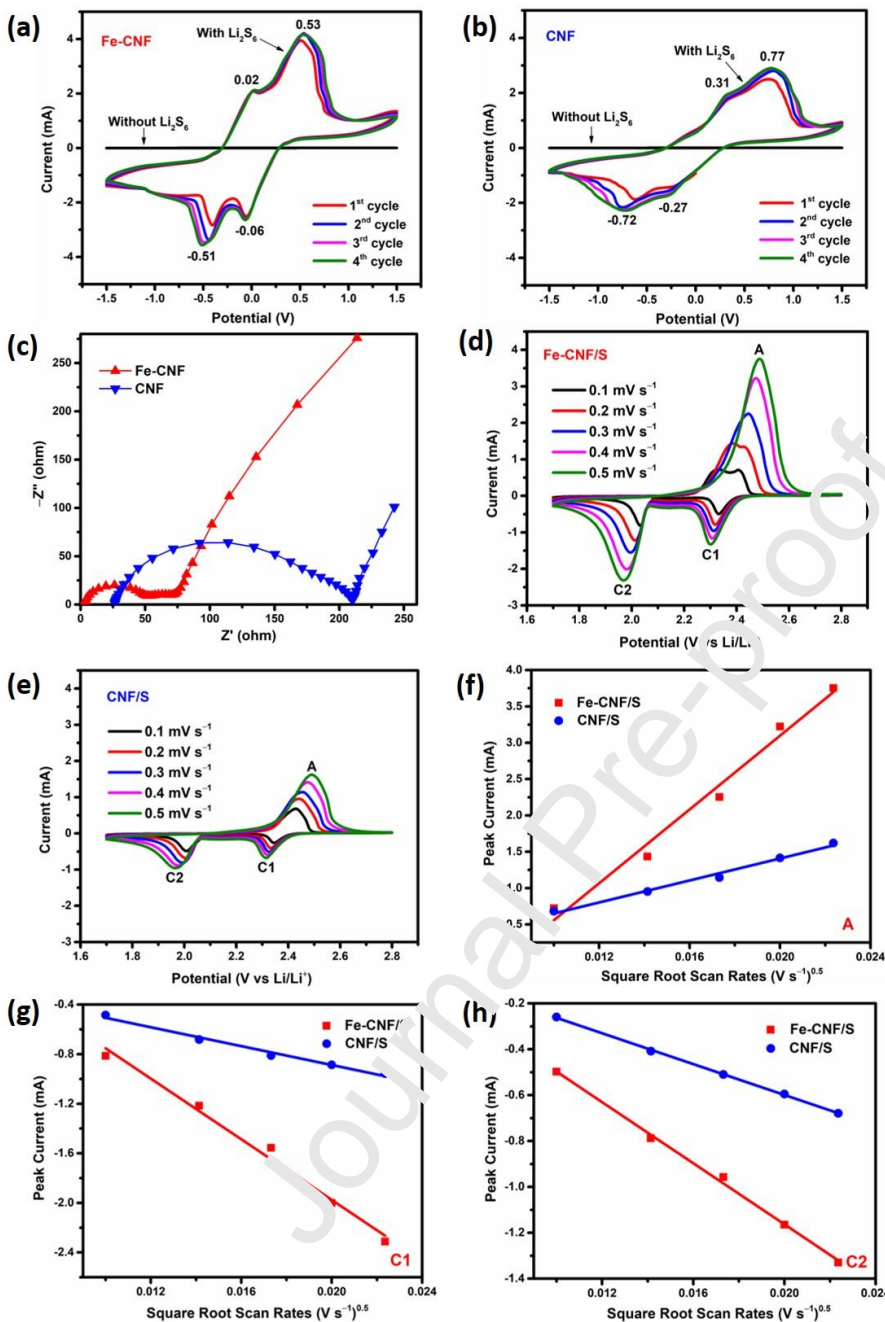


Fig. 6. Analysis of catalytic effects and lithium-ion diffusion. CV curves of symmetric cells of (a) Fe-CNF and (b) CNF electrodes without and with 0.2M Li_2S_6 at a scan rate of 10 mV s^{-1} ; (c) Nyquist plots of Fe-CNF and CNF symmetrical cells; CV curves at scan rates of $0.1\text{--}0.5 \text{ mV s}^{-1}$ of (d) Fe-CNF/S and (e) CNF/S half-cells; (f-h) Current values of peaks A, C1 and C2 in the CV curves for Fe-CNF/S and CNF/S half-cells versus the square root of scan rates.

The above results mutually demonstrate that the facile electrode design is the rationale behind the superior electrochemical performance of Fe-CNF/S. In essence, Fe-CNF/S possess following advantages: (1) The enhanced chemisorption of LiPS by the combined effect of the α -Fe₂O₃ and N-doped carbon together with the physical confinement by the interwoven nanofiber matrix strongly suppresses the shuttle effect, which accounts for the improved cycling performance. (2) High specific surface area along with adequate free space in the inter-fiber voids provide enough surfaces to interact with LiPS, enhance the electrolyte penetration and Li⁺ diffusion in the bulk of the electrode, and accommodate the significant change in volume. (3) The binder-free feature, catalytic α -Fe₂O₃ and conductive N-doped carbonaceous framework altogether provides the effective charge-transport path, promotes the rapid conversion of soluble higher order LiPS to lower order insoluble sulfides and vice versa, resulting in an improved reaction kinetics and, therefore, manifesting an improvement in specific capacity and rate capability. These structural advantages benefit the performance of LSB with Fe-CNF/S electrode even at higher current rate of 1 C as shown in Fig. 7. The initial discharge capacity reached up to 729.3 mAh g⁻¹ and 43.1% capacity was still retained after 50 cycles with an average capacity fading of 0.087% per cycle. Although, due to the presence of large-sized sulfur aggregates in the fresh Fe-CNF/S electrodes, its initial discharge capacity at different current densities could not be considered as exceptionally high in comparison to most previously reported values, however, the cycle performance of Fe-CNF/S is superior to that of most cathodes with similar mass loading reported in previous literatures (Table S2, supplementary information). In view of the superior cycle performance, a high-sulfur loading electrode (~2 mg cm⁻²) prepared by combining two electrodes of Fe-CNF/S in a layer-by-layer configuration was also tested. The double layered cathode delivered an acceptable discharge capacity of 410.6 mAh g⁻¹ at 1 C-rate with an

excellent reversible capacity of 287.5 mAh g^{-1} , corresponding to an average capacity fading of 0.107% per cycle (Fig. S11, supplementary information).

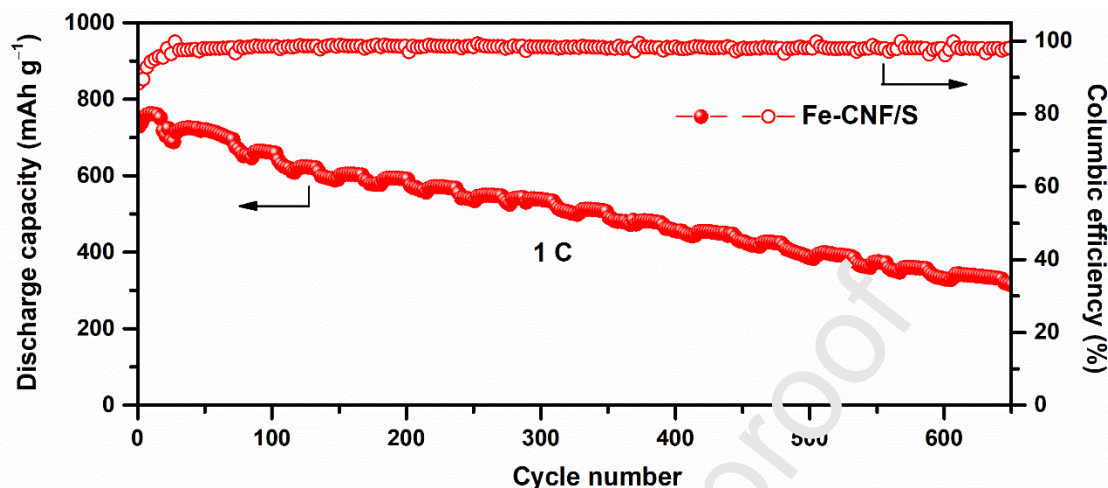


Fig. 7. Cycle performance of Fe-CNF/S electrode at 1 C-rate.

4. Conclusions

In summary, a current collector-free and binder-free flexible Fe-CNF/S electrode was fabricated using a simple method to realize improved specific capacity, cycle stability, and rate capability. After systematically comparing the electrochemical results with CNF/S and CB/S, the possible reason for enabling a better electrochemical performance in Fe-CNF/S electrode is ascribed to the strong LiPS adsorption by the combined effect of $\alpha\text{-Fe}_2\text{O}_3$ and N-doped carbon with the aid of physical restriction by the interwoven Fe-CNF matrix toward LiPS diffusion. In addition, the efficient electrolyte penetration and Li^+ diffusion into the bulk of electrode, and catalytic conversion of LiPSs by $\alpha\text{-Fe}_2\text{O}_3$ and N-doped carbon framework collectively improve the performance of LSB. More importantly, such an approach avoids the fabrication difficulties associated with conventional slurry coated electrodes and therefore, could significantly reduce the manufacturing cost. This study could introduce new ways to employ simple fabrication

routes for developing various flexible architectures which deserve to be explored for next generation flexible energy storage systems.

Supplementary information

Synthesis of sulfur, Transformation of $\text{FeSO}_4 \cdot 7\text{H}_2\text{O}$ to $\alpha\text{-Fe}_2\text{O}_3$ during carbonization, SEM image of CNF nanofibrous mat with inset showing the image at higher magnification; SEM image of the top view of CNF/S electrode; XRD pattern of CNF showing a broad peak at 25° ; TGA thermogram of Fe-CNF/S electrode; Elemental mapping of Fe-CNF/S electrode after 50 cycles showing uniform distribution of Fe, C and S; High-resolution Fe 2p and N 1s spectrum of Fe-CNF/S electrode after 50 cycles of discharging-charging at 0.2 C-rate; Low magnification and high-magnification FESEM image of Fe-CNF/S electrode after 150 cycles at the discharged state of 1.7 V; Cycle performance of various cathodes developed for LSBs reported in previous literatures; Cycle performance at 1 C-rate of a double-layer Fe-CNF/S electrode having a sulfur loading of $\sim 2 \text{ mg cm}^{-2}$.

Conflicts of interest

There are no conflicts to declare

Acknowledgement

This work was supported by the Department of Science and Technology, India (Project No. DST/TMD/MES/2k17/73). The authors thank Materials Research Centre at Malviya National institute of Technology Jaipur for helping with the XPS measurements.

References

- [1] A. Rosenman, E. Markevich, G. Salitra, D. Aurbach, A. Garsuch, F.F. Chesneau, Review on Li-Sulfur Battery Systems: an Integral Perspective, *Advanced Energy Materials*. 5 (2015) 1500212. doi:10.1002/aenm.201500212.

- [2] J. Wang, G. Yang, J. Chen, Y. Liu, Y. Wang, C. Lao, K. Xi, D. Yang, C.J. Harris, W. Yan, S. Ding, R.V. Kumar, Flexible and High-Loading Lithium–Sulfur Batteries Enabled by Integrated Three-In-One Fibrous Membranes, *Advanced Energy Materials*. 9 (2019) 1902001. doi:10.1002/aenm.201902001.
- [3] J. Zhang, H. Huang, J. Bae, S.-H. Chung, W. Zhang, A. Manthiram, G. Yu, Nanostructured Host Materials for Trapping Sulfur in Rechargeable Li-S Batteries: Structure Design and Interfacial Chemistry, *Small Methods*. 2 (2018) 1700279. doi:10.1002/smtd.201700279.
- [4] D.-W. Wang, Q. Zeng, G. Zhou, L. Yin, F. Li, H.-M. Cheng, I.R. Gentle, G.Q.M. Lu, Carbon–sulfur composites for Li–S batteries: status and prospects, *Journal of Materials Chemistry A*. 1 (2013) 9382. doi:10.1039/c3ta11045a.
- [5] R. Fang, S. Zhao, Z. Sun, D.-W. Wang, H.-M. Cheng, F. Li, More Reliable Lithium-Sulfur Batteries: Status, Solutions and Prospects, *Advanced Materials*. 29 (2017) 1606823. doi:10.1002/adma.201606823.
- [6] Y.-X. Yin, S. Xin, Y.-G. Guo, L.-J. Wan, Lithium-Sulfur Batteries: Electrochemistry, Materials, and Prospects, *Angewandte Chemie International Edition*. 52 (2013) 13186–13200. doi:10.1002/anie.201304762
- [7] Z. Cao, J. Jia, S. Chen, H. Li, M. Sang, M. Yang, X. Wang, S. Yang, Integrating Polar and Conductive Fe_2C_3 - Fe_3C Interface with Rapid Polysulfide Diffusion and Conversion for High-Performance Lithium–Sulfur Batteries, *ACS Applied Materials & Interfaces*. 11 (2019) 39772–39781. doi:10.1021/acsami.9b11419.
- [8] J. Zhang, J. Guo, Y. Xia, Y. Gan, H. Huang, C. Liang, G. Du, X. Tao, W. Zhang, Hierarchically assembled mesoporous carbon nanosheets with an ultra large pore volume for high-performance lithium–sulfur batteries, *New J. Chem.* 43 (2019) 1380–1387. doi:10.1039/C8NJ05548C.
- [9] M. Adam, P. Strubel, L. Borchardt, H. Althues, S. Dörfler, S. Kaskel, Trimodal hierarchical carbide-derived carbon monoliths from steam- and CO_2 -activated wood templates for high rate

- lithium sulfur batteries, *Journal of Materials Chemistry A*. 3 (2015) 24103–24111. doi:10.1039/C5TA06782K.
- [10] J.S. Lee, W. Kim, J. Jang, A. Manthiram, Sulfur-Embedded Activated Multichannel Carbon Nanofiber Composites for Long-Life, High-Rate Lithium-Sulfur Batteries, *Advanced Energy Materials*. 7 (2017) 1601943. doi:10.1002/aenm.201601943.
- [11] B.P. Williams, Y.L. Joo, Tunable Large Mesopores in Carbon Nanofiber Interlayers for High-Rate Lithium Sulfur Batteries, *Journal of The Electrochemical Society*. 163 (2016) A2745–A2756. doi:10.1149/2.0931613jes.
- [12] H. Wang, W. Zhang, J. Xu, Z. Guo, Advances in Polar Materials for Lithium-Sulfur Batteries, *Adv. Funct. Mater.* 28 (2018) 1707520. doi:10.1002/adfm.201707520.
- [13] G. Liang, J. Wu, X. Qin, M. Liu, Q. Li, Y.-B. He, J.-K. Kim, B. Li, F. Kang, Ultrafine TiO_2 Decorated Carbon Nanofibers as Multifunctional Interlayer for High-Performance Lithium–Sulfur Battery, *ACS Applied Materials & Interfaces*. 8 (2016) 23105–23113. doi:10.1021/acsami.6b07487.
- [14] X. Shang, P. Guo, T. Qin, M. Liu, M. Lv, D. Liu, D. He, Sulfur Immobilizer by Nanoscale TiO_2 Trapper Deposited on Hierarchical Porous Carbon and Graphene for Cathodes of Lithium-Sulfur Batteries, *Advanced Materials Interfaces*. 5 (2018) 1701602. doi:10.1002/admi.201701602.
- [15] Y. Kong, J. Luo, C. Jin, H. Yuan, O. Sheng, L. Zhang, C. Fang, W. Zhang, H. Huang, Y. Xia, C. Liang, J. Zhang, Y. Gan, X. Tao, Enhanced sulfide chemisorption by conductive Al-doped ZnO decorated carbon nanoflakes for advanced Li–S batteries, *Nano Research*. 11 (2018) 477–489. doi:10.1007/s12274-017-1655-7.
- [16] X. Tao, J. Wang, C. Liu, H. Wang, H. Yao, G. Zheng, Z.W. Seh, Q. Cai, W. Li, G. Zhou, C. Zu, Y. Cui, Balancing surface adsorption and diffusion of lithium-polysulfides on nonconductive oxides for lithium–sulfur battery design, *Nature Communications*. 7 (2016). doi:10.1038/ncomms11203.
- [17] J. Zheng, J. Tian, D. Wu, M. Gu, W. Xu, C. Wang, F. Gao, M.H. Engelhard, J.-G. Zhang, J. Liu, J. Xiao, Lewis Acid–Base Interactions between Polysulfides and Metal Organic Framework in Lithium Sulfur Batteries, *Nano Letters*. 14 (2014) 2345–2352. doi:10.1021/nl404721h.

- [18] W. Li, Q. Zhang, G. Zheng, Z.W. Seh, H. Yao, Y. Cui, Understanding the Role of Different Conductive Polymers in Improving the Nanostructured Sulfur Cathode Performance, *Nano Letters*. 13 (2013) 5534–5540. doi:10.1021/nl403130h.
- [19] W. Zhou, X. Xiao, M. Cai, L. Yang, Polydopamine-Coated, Nitrogen-Doped, Hollow Carbon–Sulfur Double-Layered Core–Shell Structure for Improving Lithium–Sulfur Batteries, *Nano Letters*. 14 (2014) 5250–5256. doi:10.1021/nl502238b.
- [20] S. Tu, X. Chen, X. Zhao, M. Cheng, P. Xiong, Y. He, Q. Zhang, Y. Xu, A Polysulfide-Immobilizing Polymer Retards the Shuttling of Polysulfide Intermediates in Lithium–Sulfur Batteries, *Advanced Materials*. 30 (2018) 1804581. doi:10.1002/adma.201804581.
- [21] A. Raulo, S. Bandyopadhyay, S. Ahamad, A. Gupta, R. Srivastava, P. Formanek, B. Nandan, Bio-inspired poly(3,4-ethylenedioxythiophene): Poly(styrene sulfonate)-sulfur@polyacrylonitrile electrospun nanofibers for lithium-sulfur batteries, *Journal of Power Sources*. 431 (2019) 250–258. doi:10.1016/j.jpowsour.2019.05.055.
- [22] H. Al Salem, G. Babu, C. V. Rao, L.M.R. Arava, Electrocatalytic Polysulfide Traps for Controlling Redox Shuttle Process of Li–S Batteries, *Journal of the American Chemical Society*. 137 (2015) 11542–11545. doi:10.1021/ja51304472.
- [23] S. Huang, Y. Wang, J. Hu, Y.V. Lim, D. Kong, Y. Zheng, M. Ding, M.E. Pam, H.Y. Yang, Mechanism Investigation of High-Performance Li–Polysulfide Batteries Enabled by Tungsten Disulfide Nanopetals, *ACS Nano*. 12 (2018) 9504–9512. doi:10.1021/acsnano.8b04857.
- [24] H. Zhang, M. Zou, W. Zhao, Y. Wang, Y. Chen, Y. Wu, L. Dai, A. Cao, Highly Dispersed Catalytic Co_3S_4 among a Hierarchical Carbon Nanostructure for High-Rate and Long-Life Lithium–Sulfur Batteries, *ACS Nano*. 13 (2019) 3982–3991. doi:10.1021/acsnano.8b07843.
- [25] Y.-J. Zhang, J. Qu, Q.-Y. Ji, T.-T. Zhang, W. Chang, S.-M. Hao, Z.-Z. Yu, Freestanding cellulose paper-derived carbon/Fe/Fe₃C with enhanced electrochemical kinetics for high-performance lithium-sulfur batteries, *Carbon*. 155 (2019) 353–360. doi:10.1016/j.carbon.2019.08.065.

- [26] Y. Wu, X. Zhu, P. Li, T. Zhang, M. Li, J. Deng, Y. Huang, P. Ding, S. Wang, R. Zhang, J. Lu, G. Lu, Y. Li, Y. Li, Ultradispersed WxC nanoparticles enable fast polysulfide interconversion for high-performance Li-S batteries, *Nano Energy*. 59 (2019) 636–643. doi:10.1016/j.nanoen.2019.03.015.
- [27] C. Zheng, S. Niu, W. Lv, G. Zhou, J. Li, S. Fan, Y. Deng, Z. Pan, B. Li, F. Kang, Q.-H. Yang, Propelling polysulfides transformation for high-rate and long-life lithium–sulfur batteries, *Nano Energy*. 33 (2017) 306–312. doi:10.1016/j.nanoen.2017.01.040.
- [28] T.-G. Jeong, D.S. Choi, H. Song, J. Choi, S.-A. Park, S.H. Oh, H. Kim, Y. Jung, Y.-T. Kim, Heterogeneous Catalysis for Lithium–Sulfur Batteries: Enhanced Rate Performance by Promoting Polysulfide Fragmentations, *ACS Energy Letters*. 2 (2017) 327–333. doi:10.1021/acseenergylett.6b00603.
- [29] Z. Sun, J. Zhang, L. Yin, G. Hu, R. Fang, H.-M. Cheng, F. Li, Conductive porous vanadium nitride/graphene composite as chemical anchor of polysulfides for lithium-sulfur batteries, *Nature Communications*. 8 (2017). doi:10.1038/ncomms14627.
- [30] K. Xiao, J. Wang, Z. Chen, Y. Qian, Z. Liu, L. Zhang, X. Chen, J. Liu, X. Fan, Z.X. Shen, Improving Polysulfides Adsorption and Redox Kinetics by the Co_4N Nanoparticle/N-Doped Carbon Composites for Lithium-Sulfur Batteries, *Small*. 15 (2019) 1901454. doi:10.1002/smll.201901454.
- [31] Y.-S. Su, A. Manthiram, A facile in situ sulfur deposition route to obtain carbon-wrapped sulfur composite cathodes for lithium–sulfur batteries, *Electrochimica Acta*. 77 (2012) 272–278. doi:10.1016/j.electacta.2012.06.002.
- [32] F. He, G. Chen, Y. Yu, S. Hao, Y. Zhou, Y. Zheng, Facile Approach to Synthesize g-PAN/g- C_3N_4 Composites with Enhanced Photocatalytic H_2 Evolution Activity, *ACS Appl. Mater. Interfaces*. 6 (2014) 7171–7179. doi:10.1021/am500198y.
- [33] Y. Li, Y. Huang, Y. Zheng, R. Huang, J. Yao, Facile and efficient synthesis of $\alpha\text{-Fe}_2\text{O}_3$ nanocrystals by glucose-assisted thermal decomposition method and its application in lithium ion batteries, *Journal of Power Sources*. 416 (2019) 62–71. doi:10.1016/j.jpowsour.2019.01.080.

- [34] X. Zhang, L. Li, Y. Guo, D. Liu, T. You, Amorphous flower-like molybdenum-sulfide-@-nitrogen-doped-carbon-nanofiber film for use in the hydrogen-evolution reaction, *Journal of Colloid and Interface Science*. 472 (2016) 69–75. doi:10.1016/j.jcis.2016.03.041.
- [35] A.L.M. Reddy, A. Srivastava, S.R. Gowda, H. Gullapalli, M. Dubey, P.M. Ajayan, Synthesis Of Nitrogen-Doped Graphene Films For Lithium Battery Application, *ACS Nano*. 4 (2010) 6337–6342. doi:10.1021/nn101926g.
- [36] H. Liu, Y. Zhang, J. Dong, T. Ye, J. Hao, Y. Yang, X. Jiang, X. Kong, Y. Bando, X. Wang, Curving effects of concave dodecahedral nanocarbons enable enhanced Li-ion storage, *J. Mater. Chem. A*. 6 (2018) 14894–14902. doi:10.1039/C8TA04934C.
- [37] L.-C. Yin, J. Liang, G.-M. Zhou, F. Li, R. Saito, H. M. Cheng, Understanding the interactions between lithium polysulfides and N-doped graphene using density functional theory calculations, *Nano Energy*. 25 (2016) 203–210. doi:10.1016/j.nanoen.2016.04.053.
- [38] J. Zhang, H. Huang, Y. Xia, C. Liang, Y. Gan, X. Tao, W. Zhang, Enhanced Electrochemical Performance of Lithium–Sulfur Batteries with Surface Copolymerization of Cathode, *J. Electrochem. Soc.* 166 (2019) A5349–A5353. doi:10.1149/2.0531903jes.
- [39] F. Sun, J. Wang, H. Chen, W. Li, W. Qiao, D. Long, L. Ling, High Efficiency Immobilization of Sulfur on Nitrogen-Enriched Mesoporous Carbons for Li–S Batteries, *ACS Appl. Mater. Interfaces*. 5 (2013) 5630–5638. doi:10.1021/am400958x.
- [40] S. Ruan, Z. Huang, W. Cai, C. Ma, X. Liu, J. Wang, W. Qiao, L. Ling, Enabling rapid polysulfide conversion kinetics by using functionalized carbon nanosheets as metal-free electrocatalysts in durable lithium-sulfur batteries, *Chemical Engineering Journal*. 385 (2020) 123840. doi:10.1016/j.cej.2019.123840.
- [41] H. Xu, Q. Jiang, B. Zhang, C. Chen, Z. Lin, Integrating Conductivity, Immobility, and Catalytic Ability into High-N Carbon/Graphene Sheets as an Effective Sulfur Host, *Adv. Mater.* 32 (2020) 1906357. doi:10.1002/adma.201906357.

- [42] J. Song, J. Zheng, R. Zhang, S. Fu, C. Zhu, S. Feng, J.-S. McEwen, D. Du, X. Li, Y. Lin, Enhancing Chemical Interaction of Polysulfide and Carbon through Synergetic Nitrogen and Phosphorus Doping, *ACS Sustainable Chem. Eng.* 8 (2020) 806–813. doi:10.1021/acssuschemeng.9b04719.
- [43] L. Bao, J. Yao, S. Zhao, Y. Lu, Y. Su, L. Chen, C. Zhao, F. Wu, Densely Packed 3D Corrugated Papery Electrodes as Polysulfide Reservoirs for Lithium–Sulfur Battery with Ultrahigh Volumetric Capacity, *ACS Sustainable Chem. Eng.* 8 (2020) 5648–5661. doi:10.1021/acssuschemeng.0c00243.
- [44] S.-K. Park, J.-K. Lee, Y.C. Kang, Yolk-Shell Structured Assembly of Bamboo-Like Nitrogen-Doped Carbon Nanotubes Embedded with Co Nanocrystals and Their Application as Cathode Material for Li-S Batteries, *Adv. Funct. Mater.* 28 (2018) 1705264. doi:10.1002/adfm.201705264.
- [45] J. Zhang, Y. Shi, Y. Ding, W. Zhang, G. Yu, In Situ Reactive Synthesis of Polypyrrole-MnO₂ Coaxial Nanotubes as Sulfur Hosts for High-Performance Lithium–Sulfur Battery, *Nano Lett.* 16 (2016) 7276–7281. doi:10.1021/acs.nanolett.6b05549.
- [46] S. Tu, X. Chen, X. Zhao, M. Cheng, P. Zhou, Y. He, Q. Zhang, Y. Xu, A Polysulfide-Immobilizing Polymer Retards the Shuttling of Polysulfide Intermediates in Lithium-Sulfur Batteries, *Adv. Mater.* 30 (2018) 1804581. doi:10.1002/adma.201804581.
- [47] W.-T. Tsou, C.-Y. Wu, H. Yang, J.-G. Duh, Improving the electrochemical performance of Lithium–Sulfur batteries using an Nb-Doped TiO₂ additive layer for the chemisorption of lithium polysulfides, *Electrochimica Acta.* 285 (2018) 16–22. doi:10.1016/j.electacta.2018.07.214.
- [48] J. Zhang, Y. Shi, Y. Ding, L. Peng, W. Zhang, G. Yu, A Conductive Molecular Framework Derived Li₂S/N,P-Codoped Carbon Cathode for Advanced Lithium-Sulfur Batteries, *Adv. Energy Mater.* 7 (2017) 1602876. doi:10.1002/aenm.201602876.
- [49] J.-Q. Huang, B. Zhang, Z.-L. Xu, S. Abouali, M. Akbari Garakani, J. Huang, J.-K. Kim, Novel interlayer made from Fe₃C/carbon nanofiber webs for high performance lithium–sulfur batteries, *Journal of Power Sources.* 285 (2015) 43–50. doi:10.1016/j.jpowsour.2015.02.140.

- [50] H. Wu, Y. Li, J. Ren, D. Rao, Q. Zheng, L. Zhou, D. Lin, CNT-assembled dodecahedra core@nickel hydroxide nanosheet shell enabled sulfur cathode for high-performance lithium-sulfur batteries, *Nano Energy*. 55 (2019) 82–92. doi:10.1016/j.nanoen.2018.10.061.
- [51] L. Lodovico, A. Varzi, S. Passerini, Radical Decomposition of Ether-Based Electrolytes for Li-S Batteries, *J. Electrochem. Soc.* 164 (2017) A1812–A1819. doi:10.1149/2.0311709jes.
- [52] L. Tan, X. Li, Z. Wang, H. Guo, J. Wang, Lightweight Reduced Graphene Oxide@MoS₂ Interlayer as Polysulfide Barrier for High-Performance Lithium–Sulfur Batteries, *ACS Appl. Mater. Interfaces*. 10 (2018) 3707–3713. doi:10.1021/acsami.7b18645.
- [53] S. Wang, J. Liao, X. Yang, J. Liang, Q. Sun, J. Liang, F. Zhao, A. Koo, F. Kong, Y. Yao, X. Gao, M. Wu, S.-Z. Yang, R. Li, X. Sun, Designing a highly efficient polysulfide conversion catalyst with paramontroseite for high-performance and long-life lithium-sulfur batteries, *Nano Energy*. 57 (2019) 230–240. doi:10.1016/j.nanoen.2018.12.021.
- [54] H. Lin, L. Yang, X. Jiang, G. Li, T. Zhang, Q. Yao, G.W. Zheng, J.Y. Lee, Electrocatalysis of polysulfide conversion by sulfur-deficient MoS₂ nanoflakes for lithium–sulfur batteries, *Energy Environ. Sci.* 10 (2017) 1476–1486. doi:10.1039/C7EE01047H.